Supporting Information for

Probing the Site-Selective Doping in $SrSnO_3$:Eu Oxides and its Impact on the Crystal and Electronic Structures Using Synchrotron Radiation and DFT Simulations

Laís Chantelle,[†] André L. Menezes de Oliveira,[*,†,‡] Brendan J. Kennedy,[‡] Jefferson Maul,[§] Márcia R. S. da Silva,[†] Thiago M. Duarte,[†] Anderson R. Albuquerque,[∥] Júlio R. Sambrano,[⊥] Richard Landers,[#] Máximo Siu-Li, [¥] Elson Longo, [◦] and Iêda M. G. dos Santos.[†]

[†]*NPE-LACOM, Dept de Química, Universidade Federal da Paraíba, João Pessoa - PB 58051-085, Brazil.*

[‡]*School of Chemistry, The University of Sydney, Sydney – New South Wales 2006, Australia.*

[§]*Dipartimento di Chimica, Universita di Torino, via Giuria 5, 10125, Torino, Italy.*

[∥]*Instituto de Química, Universidade Federal do Rio Grande do Norte, Natal - RN 59078-970, Brazil.*

[⊥]*Grupo de Simulação e Modelagem Molecular, Universidade Estadual Paulista, Bauru – SP 17033-360, Brazil.*

[#]*Instituto de Física Gleb Wataghin, Universidade Estadual de Campinas, Campinas – SP 13083-859, Brazil.*

[¥]*Instituto de Física, Universidade de São Paulo, São Carlos - SP 13563-120, Brazil.*

[◦]*LIEC/INCTMN, Universidade Estadual Paulista, Araraquara - SP 14800-060, Brazil.*

*** Corresponding author:**

E-mail: andrel_ltm@hotmail.com; andreluiz@ccen.ufpb.br.

Tel./Fax: +55-83-32167441.

EXPERIMENTAL SECTION

Material Preparation.

$SrSnO_3$, $(Sr_{0.99}Eu_{0.01})SnO_3$ and $Sr(Sn_{0.99}Eu_{0.01})O_3$ were synthesized, for the first time, by the modified-Pechini method using cationic polymeric precursor solutions as shown in **Scheme S1-S3**. Tin chloride ($SnCl_2 \cdot 2H_2O$, *J.T.Backer* 99.9%), ammonium hydroxide (NH_4OH, PA, *Vetec*), nitric acid (HNO_3, *Dinamica* 65%), strontium nitrate ($Sr(NO_3)_2$, *Vetec* 99%), europium oxide (Eu_2O_3, *Alfa Aesar* 99.99%), monohydrated citric acid ($C_6H_8O_7 \cdot H_2O$, *Cargill* 99.5%) and ethylene glycol ($C_2H_6O_2$, *Acros* 99%) were used as starting materials.

The solutions were prepared by dissolving the metal salts in an aqueous citric acid solution 3:1 (citric acid:metal) molar ratio and ethylene glycol with 40:60 mass ratio (ethylene glycol:citric acid) under heating at 70 ºC and constant stirring. The temperature was raised to about 90 ºC to obtain polymeric resins with the desired compositions, followed by calcination in air at 300 ºC for 1 h to obtain the precursor powders. The powders were grinded for 10 min in a SPEX planetary mill using two 6 mm dia. tungsten carbide balls. Further calcination at 250 ºC was performed in an oxidizing atmosphere for 12 h, at a flow rate of 2.5 mL min^{-1}, to eliminate the organic matter. Finally, the precursor powders were calcined in air at 700 ºC for 4 h in order to obtain the desired perovskite phase. Similar synthesis procedure can be found in previous works.[1-3] It is worth mentioning the synthesis of $(Sr_{0.99}Eu_{0.01})SnO_3$ and $Sr(Sn_{0.99}Eu_{0.01})O_3$ compounds was done by exchanging the order of reagent addition to direct the Eu^{3+} ions to two distinct sites (dodecahedral and octahedral) in $SrSnO_3$ as shown in **Schemes S2** and **S3**.

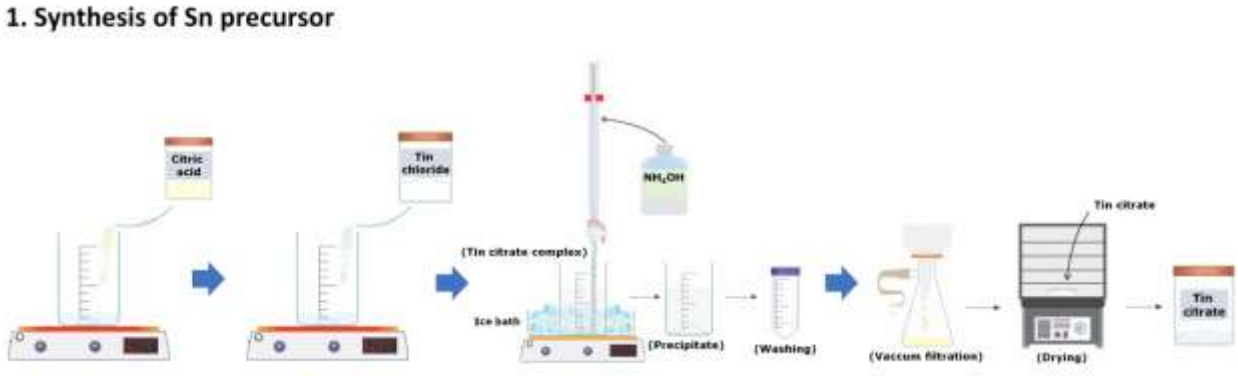

Scheme S1. Synthesis of tin precursor.

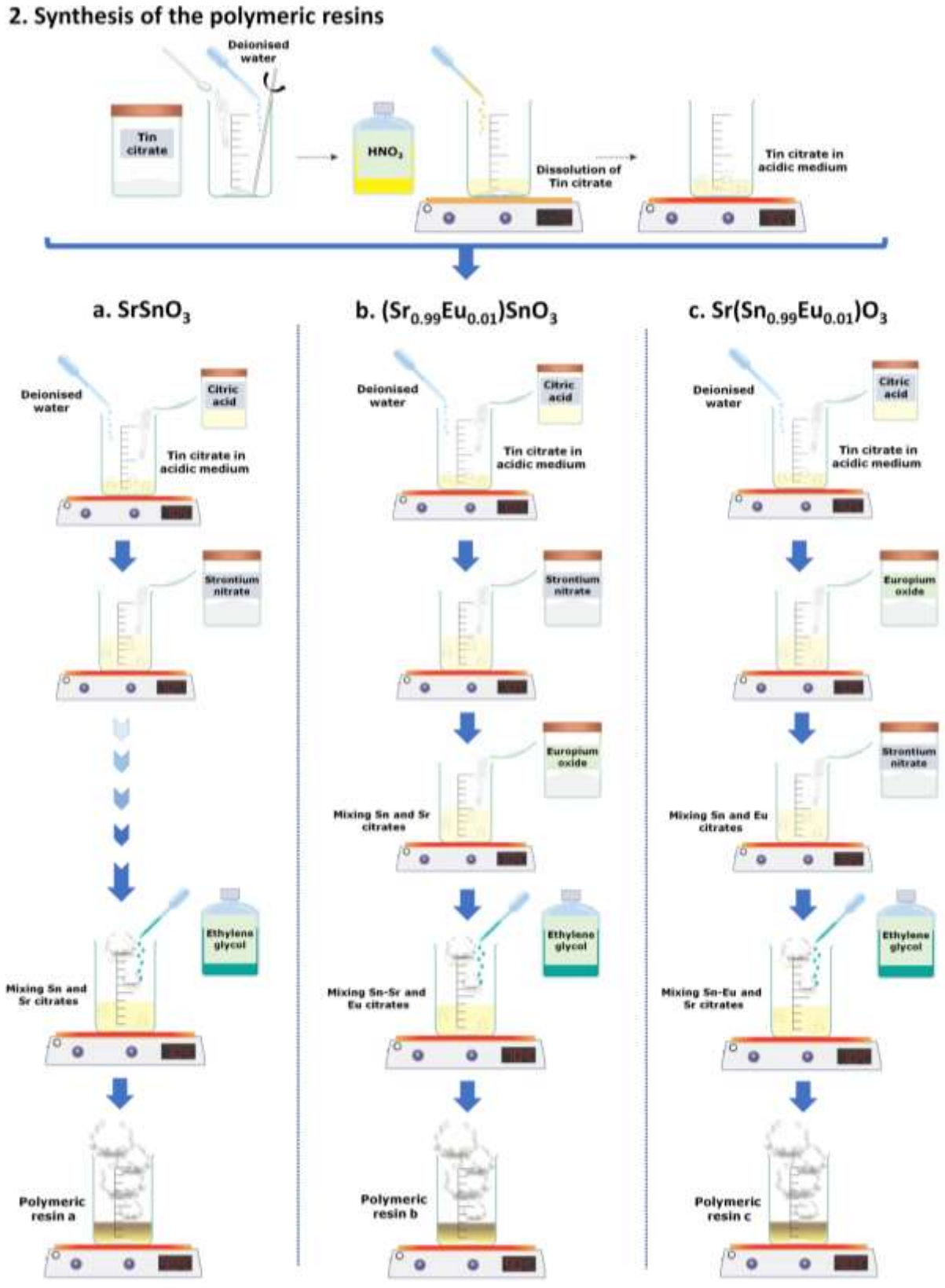

Scheme S2. Synthesis of the polymeric precursor resins.

3. Thermal treatments to obtain the solid perosvskite oxides

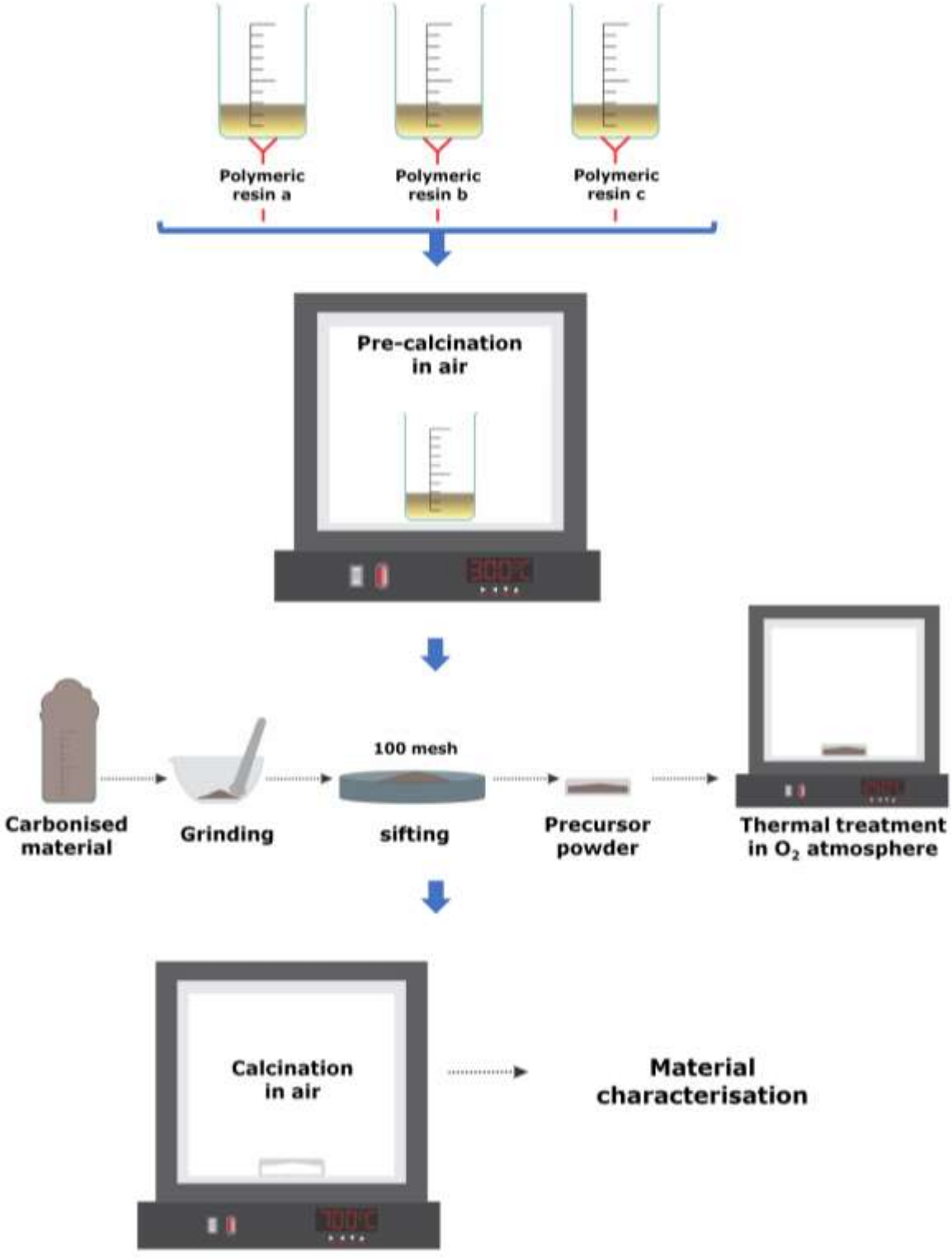

Scheme S3. Thermal treatments for the crystallization of perovskite oxides.

Material Characterization

The synthesized materials were systematically characterized by a combination of synchrotron X-ray powder diffraction (S-XRD), X-ray fluorescence (XRF), infrared (IR) and Raman spectroscopy, X-ray absorption near edge spectroscopy (XANES), X-ray photoelectron spectroscopy (XPS), Electron Paramagnetic Resonance (EPR), UV-vis and photoluminescence (PL) spectroscopy. In addition, the surface charge properties of the materials have been evaluated using Zeta Potential measurements.

Firstly, the europium content was determined by X-ray fluorescence using an XRF-1800 Shimadzu spectrometer. Infrared (IR) analyses were carried out in an IRPrestige-21 Shimadzu spectrophotometer, using KBr pellets, in the range of 2000-400 cm^{-1}. Raman measurements were performed using a WITec Scanning Near-Field Optical Microscope Alpha 300 S System. The spectra were acquired using a 514 nm Nd:YAG laser at 150 mW with about 4 cm^{-1} resolution. The XPS spectra were obtained with a VSW HA-100 spherical analyzer using an AlKα radiation ($h\nu$ = 1486.6 eV).The high-resolution spectra were measured with constant analyzer pass energies of 44 eV, (which produces a full width at half-maximum (FWHM) line width of 1.6 eV for the Au($4f_{7/2}$) line).The pressure during the measurements was always lower than 6×10^{-8} mbar. The powdered samples were pressed on to carbon double-faced tape fixed to a stainless steel sample holder and analyzed without further preparation. Surface charging was corrected shifting all spectra so that the C1*s* line due to adventitious carbon was at 284.6eV. Curve fitting was performed using Gaussian line shapes, and a Shirley background was subtracted from the data and where necessary X-Ray satellites were subtracted. The optical and electronic properties were analyzed by ultraviolet–visible (UV–vis) absorption and photoluminescence (PL) spectroscopy. UV–vis spectra were obtained using a Shimadzu UV-2550 spectrometer in total

reflectance mode. PL measurements were performed through a Monospec 27 monochromator (Thermal Jarrel Ash, USA) coupled to a R446 photomultiplier (Hamamatsu, Japan). A krypton ion laser of 350.7 nm (Coherent Innova 90 K, USA) was used as excitation source, keeping its maximum output power at 250 mW. Electron Paramagnetic Resonance (EPR) spectra were recorded at room temperature using a Bruker EMXnano EPR spectrometer operating in the X-band (9.62 GHz) at a modulation frequency of 100 kHz. The spectrometer is equipped with an ER 4119HS resonator in the cavity. Spectrometer control was performed by the Bruker Xenon software. The point of zero charge (PCZ) of the materials was determined by potentiometric titration using a Zetasizer Nano Series with He-Ne laser of 633 nm equipped with an MPT-2 Autotritator (Malvern Panalytical, U.K.). A 0.05 g L^{-1} suspension of the different perovskites was prepared using a 0.1 mmol L^{-1} $NaNO_3$ solution. Aliquots of 10 mL of the suspensions were sonicated at room temperature and pH values were adjusted by addition of 0.1 mol L^{-1} HNO_3 or 0.1 mol L^{-1} NaOH solutions.

Synchrotron X-ray powder diffraction (S-XRD) data were collected at room temperature using the powder diffractometer at BL-10 beamline of the Australian Synchrotron.[4] The samples were ground into a very fine powder and housed in 0.2 mm glass capillaries that were rotated during the measurements according to Debye-Scherrer geometry. The energy of the beam was set to ~15 KeV (λ = 0.825939 Å) calibrated using an NIST 660b LaB_6 standard reference material. The crystal structure of the samples was then determined with Rietveld method as implemented in the GSASII software package.[5] The europium M-edge and oxygen K-edge X-ray absorption near edge spectra (XANES) were measured at the soft X-ray spectroscopy beamline of Australian Synchrotron.[6] The samples were finely dusted onto conducting carbon tape placed on a gold disk, which was inserted into the vacuum chamber via a load lock. The samples were

analyzed with a vacuum lower than 10^{-9} mbar and the spectra were collected in a total electron yield (TEY) mode in the region of 1110-1200 eV for europium M-edge and 520-600 eV for oxygen K-edge with 0.1 eV/step. All XANES spectra were normalized using the Athena software.[7]

Computational Models

In order to provide information about the site-selective doping effect on the structural configuration and electronic properties in $SrSnO_3$:Eu perovskites and to explain the rationality of the experimental results, theoretical calculations were performed based on the density functional theory (DFT) as implemented in CRYSTAL17 software.[8-11]

In the calculations, geometry optimizations were performed applying the PBE0 hybrid functional model. The band structure diagram and projected density of states (PDOS) were also obtained. In addition, the |α-β| spin density maps for Eu-doped systems are shown. At room temperature $SrSnO_3$ adopts a distorted orthorhombic structure with *Pbnm* space group. The *Pbnm*-type symmetry of $SrSnO_3$ is characterized by cooperative tilting ($a^-a^-c^+$ in Glazer notation) of the corner sharing SnO_6 octahedra. These tilts occur in consequence of the mismatch between the Sn^{4+} at octahedral sites SnO_6 and the small alkaline-eath Sr^{2+} cations that occupy the dodecahedra sites SrO_{12}.[12-13] This type of structure is illustrated in **Figure 4** in the manuscript.

Tolerance factors of 7, 7, 7, 7 and 14 were adopted as the criteria for the calculations of exchange and Coulomb integrals, assuming 10^{-7} hartree/cell factor as a convergence of electronic energy. A mesh of 8 *x 8 x* 8 *k*-points in the irreducible Brillouin zone was used for the integration into reciprocal space, selected according to Monkhorst-Pack scheme.[14] The Sr atom was described by the Hay and Wadt small core potential, with valence 10 electrons in valence shell 311/1 (sp/d), and the Sn was described by the effective core pseudopotential with 22 electrons in

valence shell 411/51 (sp/d). A small core potential for 28 electrons was adopted for the Eu atom, with the valence electrons explicitly treated in a (16sp 10d 9f)/[5sp 2d 3f] basis set. The all electron basis set O 8/411/1 (s/sp/d) was employed for the oxygen. All basis set are available in the Crystal Basis Set Library.[11] A 3.125% of Eu doping was done on a 2 *x* 2 *x* 2 supercell composed by 32 units of $SnSnO_3$ (**Figure 4** in the manuscript), where Sr and Sn atoms were replaced to form different Eu-doped systems (i.e. Eu entering the Sr^{2+}- and Sn^{4+}-sites, without distinguishing Eu^{2+} and Eu^{3+} cations). In our calculations, no type of vacancy-induced was employed to compensate the charge imbalance in the systems. The substitution energy was also calculated using the same methodology employed by Albuquerque et al.[15]–The substitution energies must be compared considering europium with the same oxidation states as they are in its corresponding oxides (preferably oxides in which Eu atoms have similar coordination as they exhibit in doped $SrSnO_3$:Eu type systems). For these, we have considered the following equations:

$$SrSnO_3 + x\ EuO \rightarrow Sr_{(1-x)}Eu_xSnO_3 + x\ SrO$$

$$SrSnO_3 + x/2\ Eu_2O_3 + x/4\ O_2 \rightarrow SrSn_{(1-x)}Eu_xO_3 + x\ SnO_2$$

Photocatalytic Experiments

Photocatalytic properties of the materials were evaluated towards Remazol Yellow dye degradation. The tests were performed in a custom-built reactor with air circulation, using three UV lamps with λ = 254 nm (Puritec HNS S 9W, OSRAM) placed on the top. For the reactions, 66.7 mg of catalyst powder was dispersed in 100 mL of the dye solution with concentration of 10 mg L^{-1} under magnetic stirring. The dye solutions were prepared at two pH 3.5 and pH 6, using a buffer of acetic acid/sodium acetate ($C_2H_4O_2/NaC_2H_3O_2$). To evaluate the photodegradation rate

of the solution, aliquots of 5 mL were withdrawn from the reaction vessel each 20 min up to 5 h. The aliquots were centrifuged at 5000 rpm for 10 min and the final solution was analyzed in a Shimadzu UV-2550 spectrophotometer. The reaction was monitored by the variation in the intensity of the band assigned to the azo group (-N=N-) of the dye, at 411 nm.[16-17] A blank analysis was done, without catalyst, and less than 6 % discoloration was observed.

Photochemical Reusability/Stability of the Catalysts

The photochemical stability and reusability of the catalysts were evaluated by repeating the photocatalytic tests 3 times with the same material retained after each cycle. The catalysts were recycled by centrifugation, washed with demonized water and dried in air at 50 °C to be reused.

Ecotoxicity Tests

Ecotoxicity of the Remazol Yellow dye solutions before and after photocatalysis was examined on brine shrimps (*Artemia salina*). These tests were performed according to the methodology described by Andrade *et al.*[18] For the experiments, *Artemia salina* eggs were incubated in a 38 g L^{-1} NaCl solution at 37 ºC for 48 h with continuous aeration. After the incubation period, the *Artemia* nauplii were separated from their eggs and the living organisms were exposed to Remazol dyes solutions (before and after been photocatalytically treated) for 24 h. Ten alive nauplii were selected and added to each test tubes containing a 2.5:2.5 mL proportion of NaCl:dye (v/v). The tests were done in triplicate and the ecotoxicity of the medium was evaluated in terms of nauplii survival, calculated from the dead ones after the exposure time. The microorganisms were considered alive all those that presented any type of movement when observed near a light source.

SUPPLEMENTATY RESULTS AND DISCUSSION

Refined Crystal Structures Showing Distortions

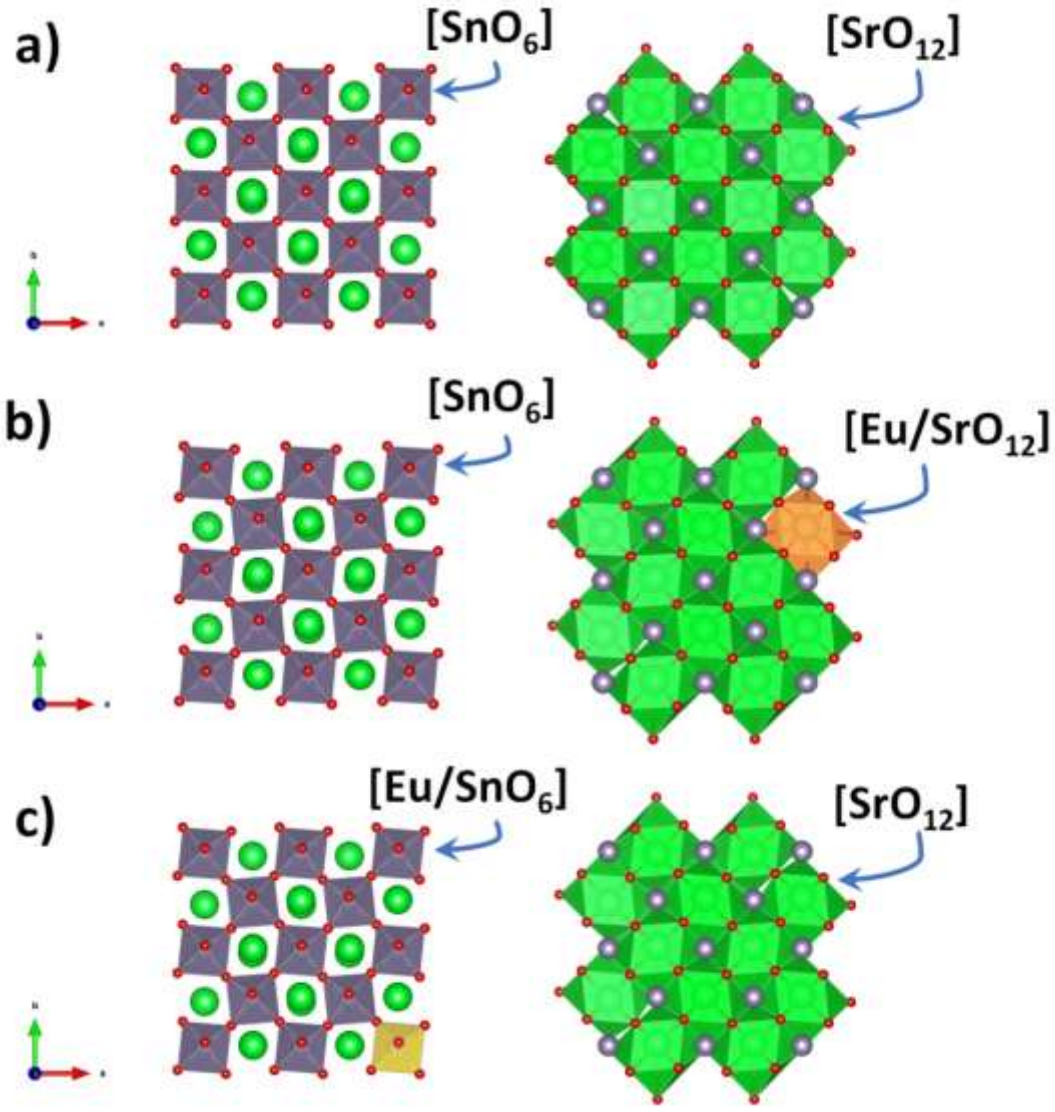

Figure S1. Representation of the refined $SrSnO_3$ (a), $(Sr_{0.99}Eu_{0.01})SnO_3$ (b) and $Sr(Sn_{0.99}Eu_{0.01})O_3$ (c) structures illustrating tilts along the *c* axes ([001] projection) drawn using the refined atomic coordinates. The $[Eu/SrO_{12}]$ polyhedra and $[Eu/SnO_6]$ octahedra of the structure are displayed as highlighted in orange and yellow, respectively. Legend: the larger green spheres represent Sr cations and smaller red spheres represent the anions, while Sn cations are the gray spheres.

Infrared Spectroscopy (IR) Analysis

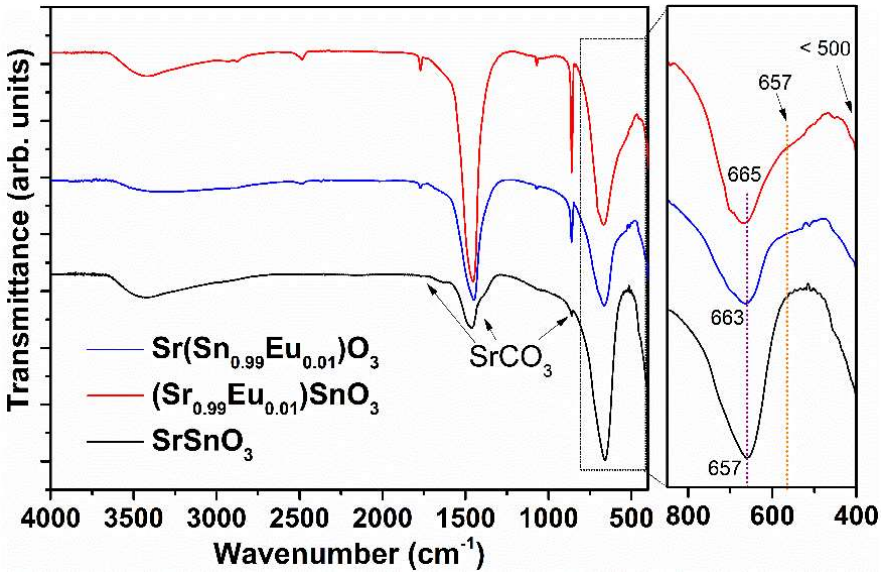

Figure S2. IR spectra of the $SrSnO_3$, $(Sr_{0.99}Eu_{0.01})SnO_3$ and $Sr(Sn_{0.99}Eu_{0.01})O_3$ samples.

IR spectra of $SrSnO_3$, $(Sr_{0.99}Eu_{0.01})SnO_3$ and $Sr(Sn_{0.99}Eu_{0.01})O_3$ were analyzed as shown in **Figure S2**. The IR modes of a *AB*O_3-type perovskite compound are found in the wavenumber range lower than 700 cm^{-1}, which are located in three regions: 80-140 cm^{-1} (ν_1 assigned to A-BO_3 lattice modes), 170-280 cm^{-1} (ν_2 related to O-B-O bending modes) and 490-680 cm^{-1} (ν_3 attributed to B-O stretching modes). Torsional modes of BO_3 group can also be observed, which may become active in perovskite with structural distortion from the ideal cubic symmetry. In orthorhombic perovskites with space group *Pbnm*, as for $SrSnO_3$, 25 modes are IR active at Γ of the Brillouin zone, which are given by the irreducible representations $\Gamma_{IR} = 9B_{1u} + 7B_{2u} + 9B_{3u}$.[1] In the present work, some of these modes were observed due to the detection limit of the IR spectrophotometer. In $SrSnO_3$, the bands centered at 667 and 540 cm^{-1} are assigned to symmetric and asymmetric Sn-O-Sn stretching vibrations in SnO_6 octahedra. These bands appeared slightly

shifted for $(Sr_{0.99}Eu_{0.01})SnO_3$ and $Sr(Sn_{0.99}Eu_{0.01})O_3$ samples, which indicates change in the symmetry of the octahedra. Similar behavior was observed Oliveira *et al*[3] for other systems. Apart from the modes of the perovskite structure, others modes are observed at 1774, 1448, 1070 and 859 cm^{-1} attributed to carbonate groups. A partial elimination of carbonate takes place especially for the $SrSnO_3$ sample in agreement with the XRD results. In addition, the broad band located around 3400 cm^{-1} corresponds to OH groups from water absorbed on the samples surface.

Raman Spectroscopy Analysis

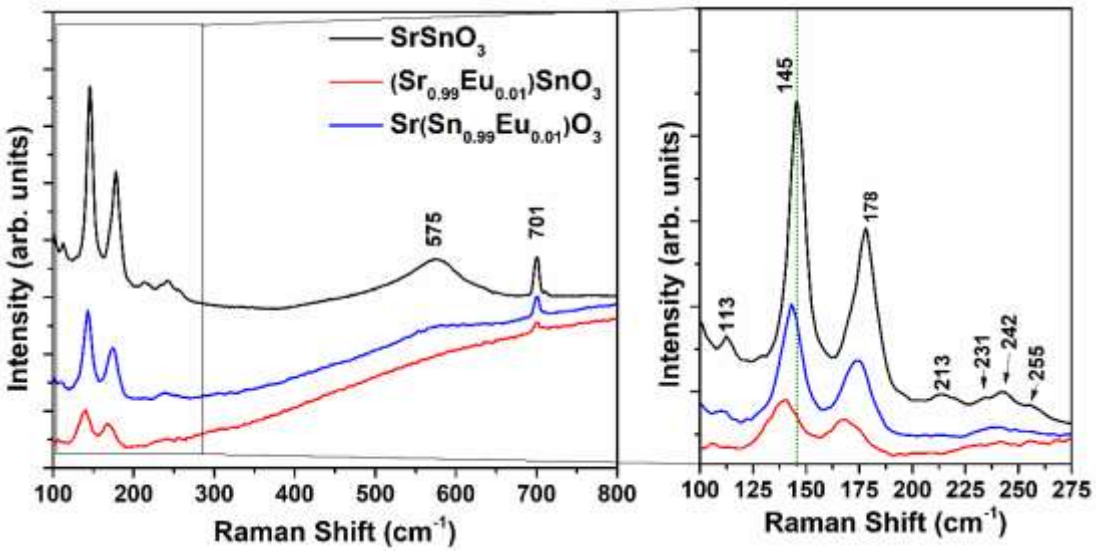

Figure S3. Raman spectra of $SrSnO_3$, $(Sr_{0.99}Eu_{0.01})SnO_3$ and $Sr(Sn_{0.99}Eu_{0.01})O_3$.

Raman spectra of the samples calcined at 700 ºC (**Figure S3**) were collected at room temperature to evaluate the local structure of the samples. The orthorhombic phase of $SrSnO_3$ perovskite has 24 active Raman modes ($\Gamma_{Raman} = 7A_g + 5B_{1g} + 7B_{2g} + 5B_{3g}$). Some of these modes may not be observed due to superposition of to a low polarisation.[19]

According to Lee *et al*,[20] in $SrSnO_3$ nanoparticles the modes assigned to Sr-SnO_3 bonds are identified at 95 and 185 cm^{-1}; while bands at 310 and 440 cm^{-1} are assigned to modes associated to the SnO_3 bonds and the bands at 470-560 cm^{-1} are due to the asymmetric stretching of the Sn-O bonds. In the present work, Raman modes assigned to the orthorhombic *Pbnm* $SrSnO_3$ were observed at 113, 145, 178, 212, 245, 254 and 575 cm^{-1}, while the band at 701 cm^{-1} was related to the presence of carbonate. Small peaks at 113 and the two highest ones at 145 and 178 cm^{-1} are attributed to B_{2g} mode, associated the lattice mode (Sr-SnO_3). The peaks observed at 212 cm^{-1}

are assigned to A_g mode, corresponding to the scissor movement of Sn-O-Sn groups along the *c* axis, while those ones at 245and 254 cm^{-1} (A_g) are assigned to the stretching of the O-Sn-O groups in the *ab* plane and to the scissor movement of the Sn-O-Sn groups perpendicular to the *c* axis. It may also be observed that band at 213 cm^{-1} disappears after Eu-doping. The peak shift and broadening observed after Eu-doping indicates a disturbance on the structure by the incorporation of Eu, suggesting Sr and Sn replacements to form $(Sr_{1-x}Eu_x)SnO_3$and $Sr(Sn_{1-x}Eu_x)O_3$ type compositions. Moreover, the Raman mode located at 575 cm^{-1} might be assigned to a higher contribution of the oxygen movement due to vacancies or other defects in the samples.

XANES Spectroscopy Analysis

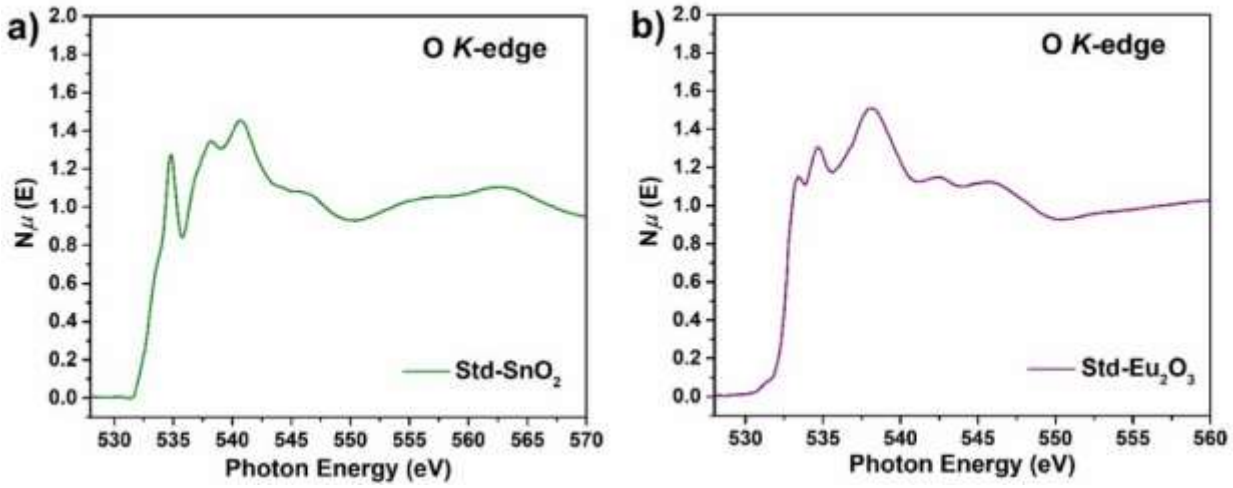

Figure S4. Normalized O K-edge XANES spectra from the SnO_2 (a) and Eu_2O_3 (b) standard samples.

XPS Spectroscopy Analysis

Figure S5 shows the XPS surveys and high resolution XP scan of Eu element in the samples. As expected, the XPS surveys (**Figure S**5a) revealed that Sr, Sn, and O elements compose the surface of the samples, but Eu also exists in the $SrSnO_3$:Eu ones. The C signal observed in XPS also confirms the existence of $SrCO_3$. The high resolution XP spectra that comprehend the Eu 3*d* are shown in **Figure S**5b and confirm the presence of Eu^{3+} cations in Eu-doped samples.

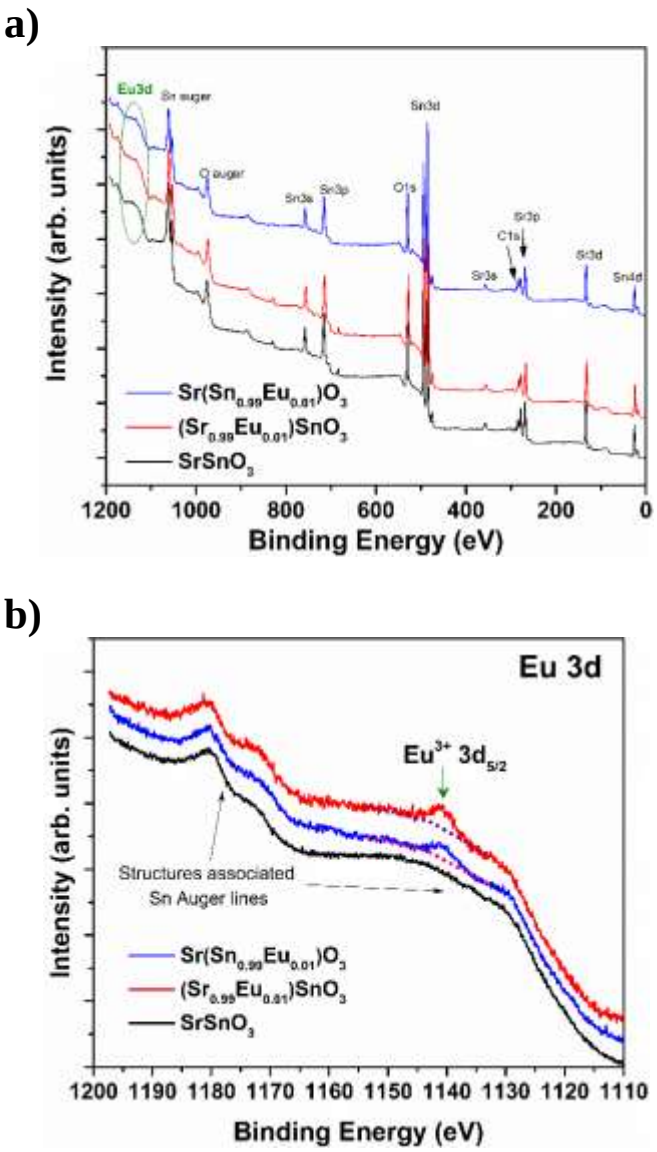

Figure S5. XPS survey spectra (a), high resolution Eu 3*d* scans for the samples.

Deep and Shallow Defects Using Photoluminescence

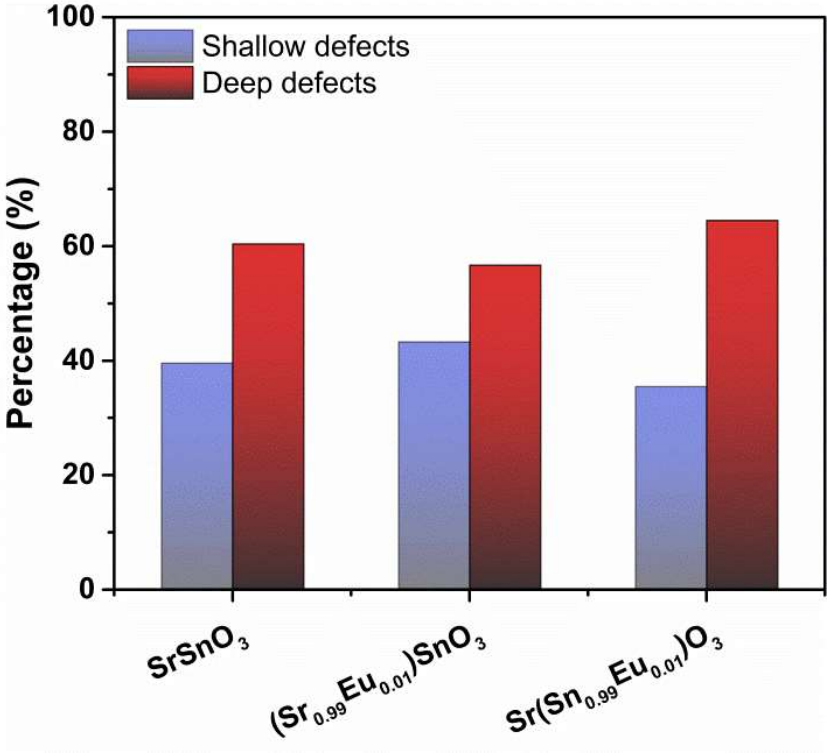

Figure S6. Evaluation of the short-range disorder using photoluminescence (deep and shallow defects concentration) in $SrSnO_3$, $(Sr_{0.99}Eu_{0.99})SnO_3$ and $Sr(Sn_{0.99}Eu_{0.01})O_3$ samples calcined at 700 °C. *The shallow defects are calculated as the sum of the blue and green emission components; ** The deep defects are calculated as the sum of the yellow to red emission components.

UV-vis Absorption Spectra of the Ramazol Yellow Dye Solutions at Different pH

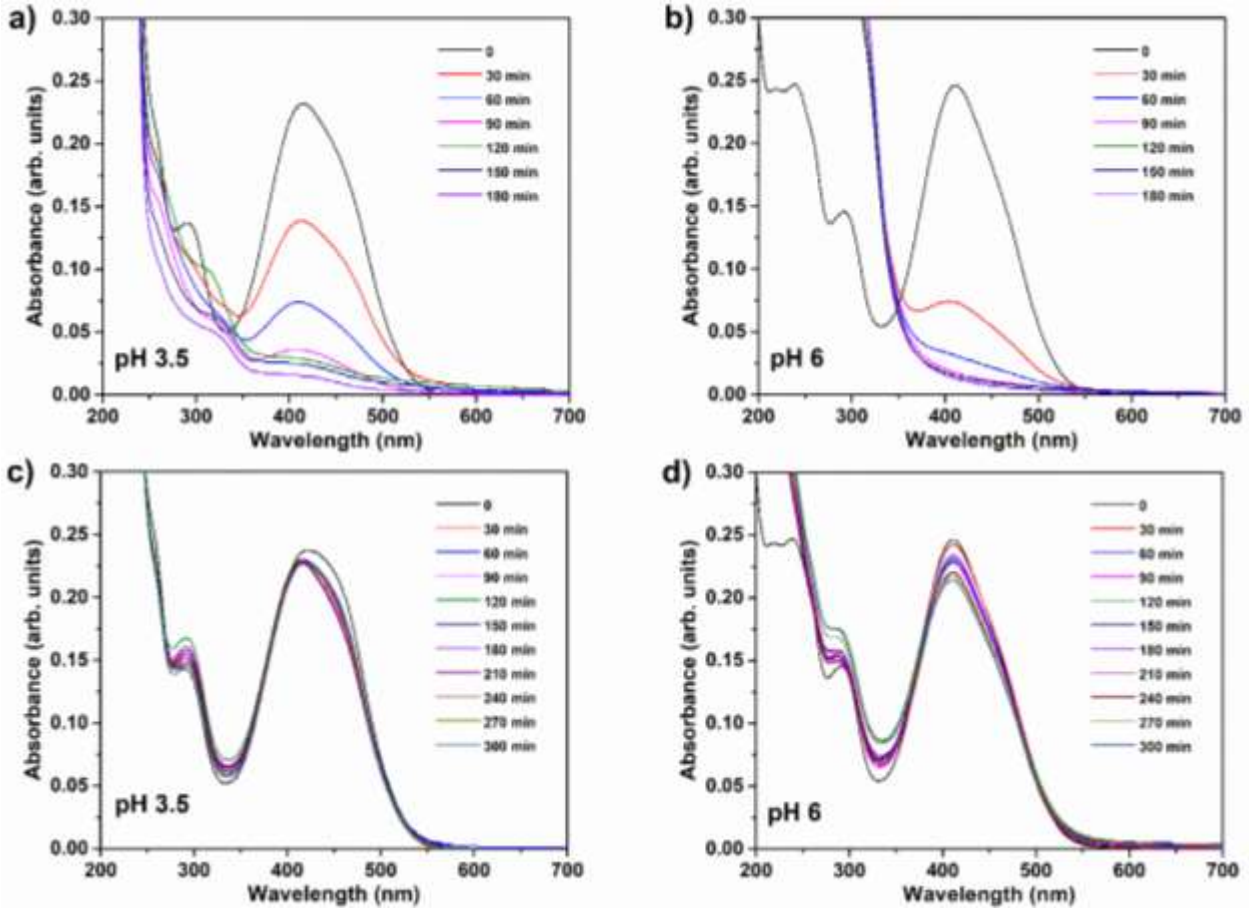

Figure S7. UV-vis absorption spectra profile of Remazol yellow as it undergoes degradation using commercial TiO_2 P25 Degussa particles as catalysts at pH 3.5(a) and 6 (b); using commercial $SrCO_3$ particles as catalysts at pH 3.5(c) and 6 (d).

UV-vis Absorption Spectra of the Ramazol Yellow Dye Solutions at Different pH

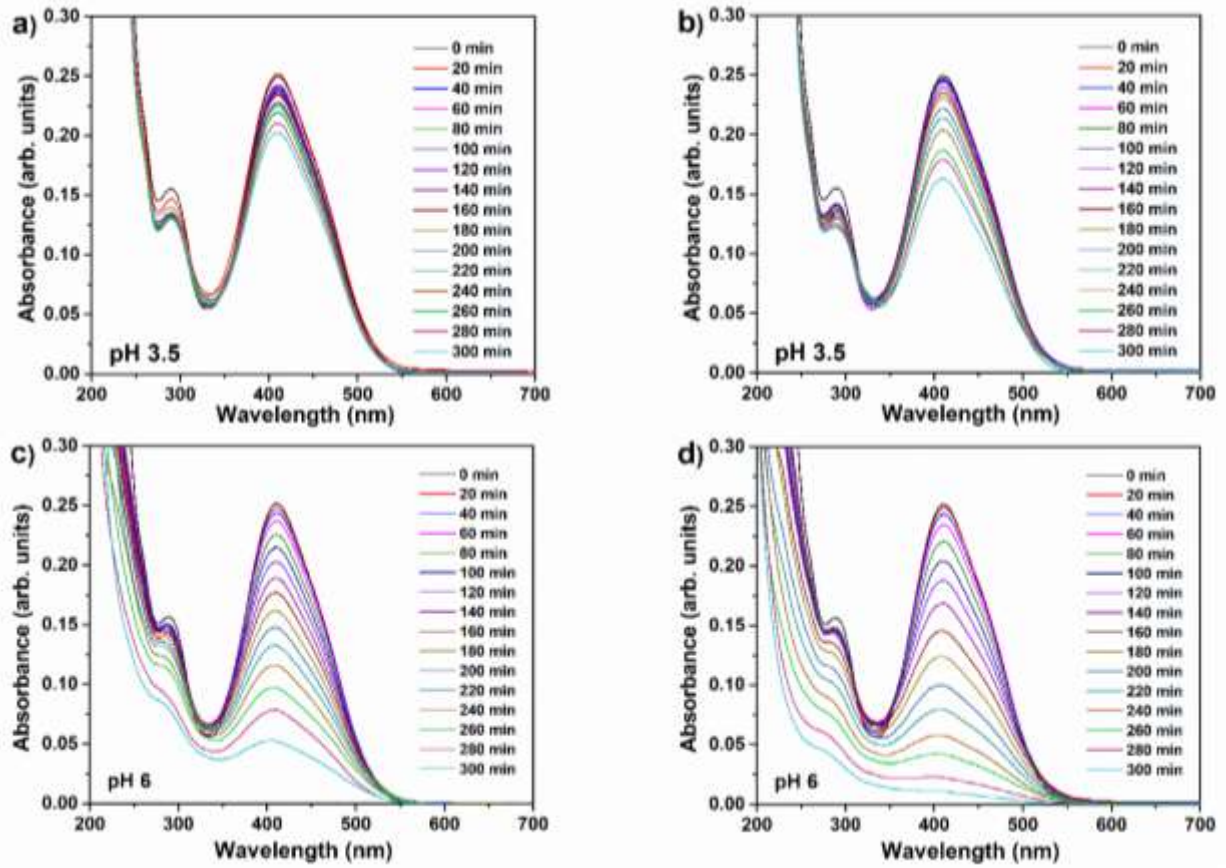

Figure S8. UV-vis absorption spectra profile of Remazol yellow as it undergoes degradation using $SrSnO_3$ (a,c) and $(Sr_{0.99}Eu_{0.01})SnO_3$ (b,d) as catalysts at pH 3.5 and 6.

Adsorption Tests in the Dark

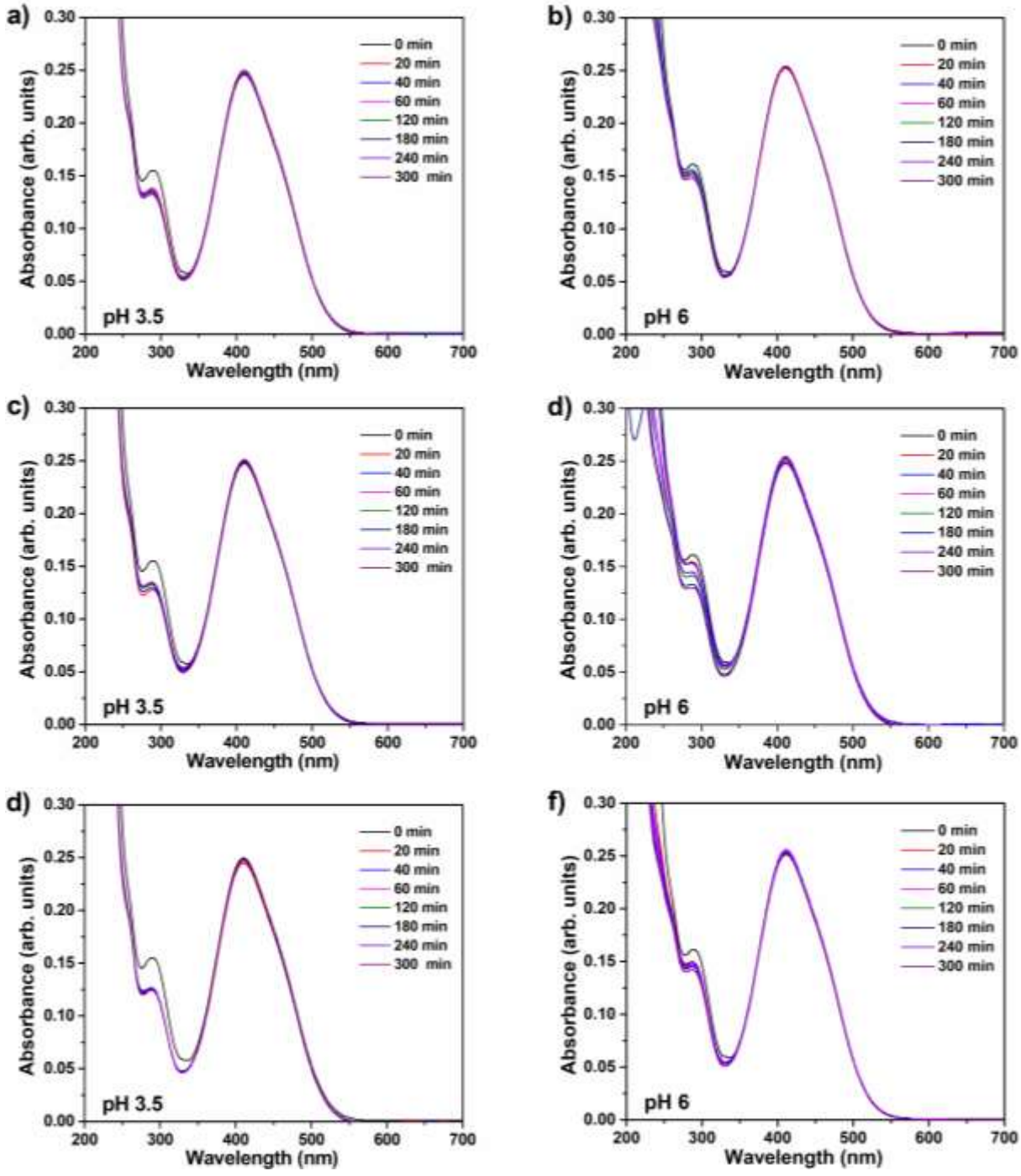

Figure S9. UV-vis absorption spectra profiles of Remazol yellow after 300 min adsorption in the dark with the presence of $SrSnO_3$ (a,b), $(Sr_{0.99}Eu_{0.01})SnO_3$ (c,d) and $Sr(Sn_{0.99}Eu_{0.01})O_3$ (e,f) catalysts at pH3.5 and pH 6.

Stability and Reusability of the Photocatalysts at pH 6

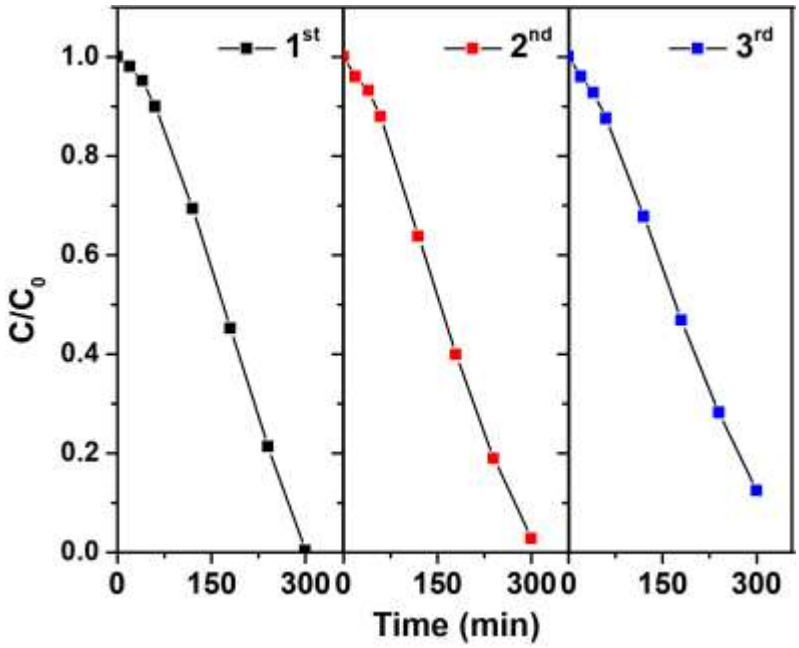

Figure S10. $Sr(Sn_{0.99}Eu_{0.01})O_3$ catalyst reuse in the photo-degradation of Remazol dye solution at pH 6.

Ecotoxicity Results

The toxicity test is considered a tool that assesses the effects of toxic agents on aquatic organisms in the control of pollution, since they are able to detect the harmful effects of pollutants in aquatic ecosystems.[21] **Figure S11** presents the mean percentage of *Artemia* survival after 24 h of contact with RNL dye solutions at pH 6 (before and after photocatalytic treatment). The results show that after 24 h the *Artemia* survivorship in the control saline solution was of 100 % and dropped to 85% when in contact with the original Remazol solution with 10 mg L^{-1} (photocatalyticaly untreated). Regarding the degraded solutions by the use of $SrSnO_3$ as catalyst, the rate of live *Artemia* was ~ 80 %, indicating a possible formation of by-products after the photocatalytic reaction. On the other hand, a higher survival percentage was observed for the Remazol solution treated using $(Sr_{0.99}Eu_{0.01})SnO_3$ and $Sr(Sn_{0.99}Eu_{0.01})O_3$ as catalysts, in which the survivorship was of 90%. The relationship of higher survival of *Artemia* might be related to the better photocatalytic performance of the Eu-containing samples, which presented efficiency of almost 100 % of dye photo-degradation. In short, the use of Eu-doped $SrSnO_3$ catalysts might not favour the formation of a more toxic media in comparison to the original untreated solution. This indicates that no by-products with toxicity indices might be forming after photocatalysis.

Ecotoxicity Using Artemia Salina

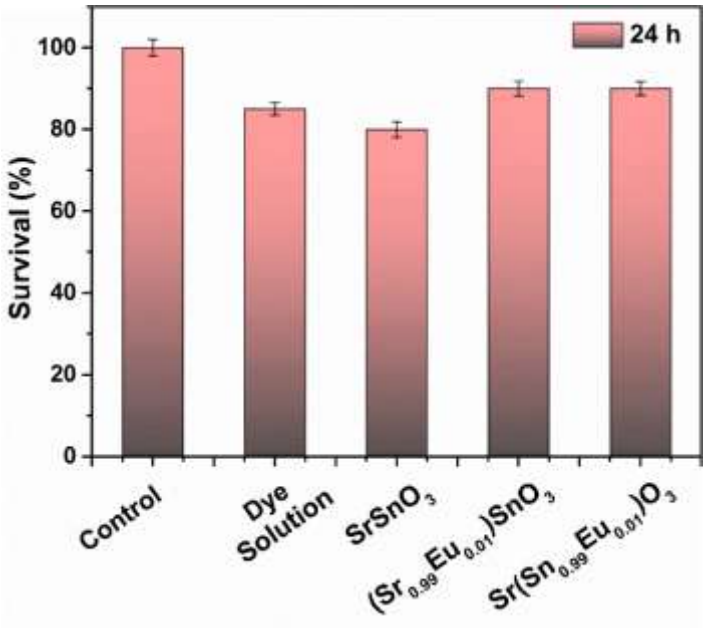

Figure S11. Percentage of *Artemia salina* survival (mean ± SD) exposed to saline solution (control), Remazol solution before photocatalysis (Dye solution) and Remazol solution photocatalytically treated using $SrSnO_3$, $(Sr_{0.99}Eu_{0.01})SnO_3$ and $Sr(Sn_{0.99}Eu_{0.01})O_3$ as catalysts.

Rietveld Refinement Data

Table S1. Room temperature unit cell parameters, atomic coordinates and atomic displacement parameters of the perovskite samples.

	$SrSnO_3$	**$(Sr_{0.99}Eu_{0.01})SnO_3$**	**$Sr(Sn_{0.99}Eu_{0.01})O_3$**
Space Group	*Pbnm* (62)	*Pbnm* (62)	*Pbnm* (62)
t	0.9609	0.9599	0.9610
a (Å)	5.7285(3)	5.7058(9)	5.7089(13)
b (Å)	5.7024(4)	5.7117(10)	5.7102(14)
c (Å)	8.05978(29)	8.0981(7)	8.0927(8)
V ($Å^3$)	263.284(8)	263.914(7)	263.813(21)
R_w(%)	3.501	4.48	4.55
GOF	2.15	3.14	2.87
A			
x	-0.0010(23)	0.0046(16)	0.002(4)
y	0.4776(6)	0.4746(4)	0.4752(5)
Uiso	0.0089(3)	0.0051(5)	0.0051(4)
B			
Uiso	0.007(0)	0.00102(18)	0.00174(16)
O1			
x	0.031(12)	-0.013(9)	0.007(20)
y	0.046(6)	0.009(3)	0.054(4)
Uiso	0.071(12)	0.002	0.002
O2			
x	0.253(8)	0.285(4)	0.277(4)
y	0.244(10)	0.225(5)	0.230(5)
z	0.0276(20)	0.0242(28)	0.0337(23)
Uiso	0.010(4)	0.010	0.0116(28)

Table S2. Selected interatomic distance Å in $SrSnO_3$, $(Sr_{0.99}Eu_{0.01})SnO_3$ and $Sr(Sn_{0.99}Eu_{0.01})O_3$.

	$SrSnO_3$	**$(Sr_{0.99}Eu_{0.01})SnO_3$**	**$Sr(Sn_{0.99}Eu_{0.01})O_3$**
A-O1	2.47(4)	2.664(20)	2.404(20)
A-O1	2.72(7)	2.81(5)	2.84(9)
A-O2	2.67(4)	2.817(26)	2.736(28)
A-O2	2.75(4)	2.614(12)	2.606(22)
A-O2	2.75(4)	2.793(27)	2.880(27)
A-O2	2.67(4)	2.793(27)	2.880(27)
A-O2	2.634(15)	2.614(12)	2.606(22)
A-O2	2.777(26)	2.817(26)	2.736(28)
Avg A-O	2.6801	2.7402	2.7110
B-O1	2 *x* 2.040(7)	2 *x* 2.0264(19)	2 *x* 2.047(4)
B-O2	2 *x* 2.02(5)	2 *x* 2.08(3)	2 *x* 2.07(3)
B-O2	2 *x* 2.04(5)	2 *x* 2.00(3)	2 *x* 2.02(3)
Avg B-O	2.0333	2.0355	2.0457

A = Sr and/or Eu*; B* = Sn and/or Eu

Table S3. Structural parameters that describe the distortion inside a [BO_6] octahedron in $SrSnO_3$, $(Sr_{0.99}Eu_{0.01})SnO_3$ and $Sr(Sn_{0.99}Eu_{0.01})O_3$ compounds. $V[BO_6]$ is the octahedron volume $[BO_6]_d/\mathring{A}^3$, ECN is the average effective coordination number, $\langle\lambda\rangle$ is the quadratic elongation, D is the distortion index and σ^2 is the average angle variation that form $O-\widehat{Sn}-O$.

	V[SnO_6]	**ECN**	$\langle\boldsymbol{\lambda}\rangle$	**D**	$\boldsymbol{\sigma^2}$
$SrSnO_3$	10.8258	5.9948	1.0256	0.00460	89.5845
$(Sr_{0.99}Eu_{0.01})SnO_3$	11.2111	5.9425	1.0038	0.01469	78.4414
$Sr(Sn_{0.99}Eu_{0.01})O_3$	11.0803	5.9733	1.0206	0.00919	71.6970

Structural Parameters Determined by Theoretical Calculations

Table S4. Calculated structural parameters for undoped and Eu-doped $SrSnO_3$ systems by DFT.

System	**Volume (Å^3)**	**Lattice parameters (Å)**		
		a	*b*	*c*
$SrSnO_3$	2135.5432	11.4639	11.4913	16.2106
$Sr(Sn_{1-y}Eu^{3+}_{y})*O_3$ - $[EuO_6]$	2135.5433	11.4639	11.4913	16.2107
$(Sr_{1-x}Eu^{2+}_{x})*SnO_3$ - $[EuO_{12}]$	2135.5433	11.4639	11.4913	16.2106

The (*) indicates the selected-site

Photoluminescence Spectra Fitting

PL spectra were fitted to the components of emission (Blue, Green, orange and Red components – **Table S5**) and classified as shallow and deep defects present above in **Figure S**6.

Table S5. Colour components contribution obtained from PL curve fitting.

	Blue		**Green**		**Yellow-orange**		**Orange-red**		**Infrared**	
	Center (nm)	%	Center (nm)	%	Center (nm)	%	Center (nm)	%	Center (nm)	%
$SrSnO_3$	460	11.3	534	28.3	603	32.2	664	17.3	728	10.9
$(Sr_{0.99}Eu_{0.01})SnO_3$	455	13.9	534	29.4	603	25.5	658	19.4	728	11.8
$Sr(Sn_{0.99}Eu_{0.01})O_3$	453	9.7	536	25.8	601	24.3	656	25.7	726	14.5

Photocatalytic Kinetics Data

Table S6. Rate constant of the photocatalytic degradation of Remazol yellow at different pH using $SrSnO_3$, $(Sr_{0.99}Eu_{0.01})SnO_3$ and $Sr(Sn_{0.99}Eu_{0.01})O_3$as catalysts.

	Rate constant, *k* (*x* 10^{-4} min^{-1})	
Catalyst	**Remazol pH6**	**Remazol pH3.5**
$SrSnO_3$	20.6 ± 0.77	4.78± 0.16
$(Sr_{0.99}Eu_{0.01})SnO_3$	28.9 ± 1.4	5.43 ± 0.59
$Sr(Sn_{0.99}Eu_{0.01})O_3$	30.1 ± 1.06	16.9 ± 1.237

REFERENCES

1. Vieira, F. T. G.; Oliveira, A. L. M. d.; Melo, D. S.; Lima, S. J. G.; Longo, E.; Maia, A. d. S.; Souza, A. G.; dos Santos, I. M. G., Crystallization study of $SrSnO_3$:Fe. *Journal of Thermal Analysis and Calorimetry* **2011,** *106*, 507-512.
2. Menezes de Oliveira, A. L.; Bouquet, V.; Dorcet, V.; Ollivier, S.; Députier, S.; Gouveia de Souza, A.; Siu-Li, M.; Longo, E.; Távora Weber, I.; Garcia dos Santos, I. M.; Guilloux-Viry, M., Evolution of the structural and microstructural characteristics of $SrSn_{1-x}Ti_xO_3$ thin films under the influence of the composition, the substrate and the deposition method. *Surface and Coatings Technology* **2017,** *313* (Supplement C), 361-373.
3. de Oliveira, A. L. M.; Silva, M. R. S.; Sales, H.; Longo, E.; Maia, A. S.; Souza, A. G.; Santos, I. M. G., Effect of the composition on the thermal behaviour of the $SrSn_{1-x}Ti_xO_3$ precursor prepared by the polymeric precursor method. *Journal of Thermal Analysis and Calorimetry* **2013,** *114* (2), 565-572.
4. Wallwork, K. S.; Kennedy, B. J.; Wang, D., The High Resolution Powder Diffraction Beamline for the Australian Synchrotron. *AIP Conference Proceedings* **2007,** *879* (1), 879-882.
5. Toby, B. H.; Von Dreele, R. B., GSAS-II: the genesis of a modern open-source all purpose crystallography software package. *Journal of Applied Crystallography* **2013,** *46* (2), 544-549.
6. Cowie, B. C. C.; Tadich, A.; Thomsen, L., The Current Performance of the Wide Range (90-2500 eV) Soft X-ray Beamline at the Australian Synchrotron. *AIP Conference Proceedings* **2010,** *1234* (1), 307-310.
7. Ravel, B.; Newville, M., ATHENA, ARTEMIS, HEPHAESTUS: data analysis for X-ray absorption spectroscopy using IFEFFIT. *Journal of Synchrotron Radiation* **2005,** *12* (4), 537-541.
8. Erba, A.; Baima, J.; Bush, I.; Orlando, R.; Dovesi, R., Large-Scale Condensed Matter DFT Simulations: Performance and Capabilities of the CRYSTAL Code. *Journal of Chemical Theory and Computation* **2017,** *13* (10), 5019-5027.
9. Dovesi, R.; Erba, A.; Orlando, R.; Zicovich-Wilson, C. M.; Civalleri, B.; Maschio, L.; Rérat, M.; Casassa, S.; Baima, J.; Salustro, S.; Kirtman, B., Quantum-mechanical condensed matter simulations with CRYSTAL. *WIREs Computational Molecular Science* **2018,** *8* (4), e1360.
10. Dovesi, R.; Saunders, V. R.; Roetti, C.; Orlando, R.; Zicovich-Wilson, C. M.; Pascale, F.; Civalleri, B.; Doll, K.; Harrison, N. M.; Bush, I. J.; D'Arco, P.; Llunell, M.; Causà, M.; Noël, Y.; Maschio, L.; Erba, A.; Rerat, M.; Casassa, S., CRYSTAL17 User's Manual. *CRYSTAL17 User's Manual, University of Torino, Torino* **2017**.
11. CRYSTAL17, *http://www.crystal.unito.it/basis-sets.php*.
12. Prodjosantoso, A. K.; Zhou, Q.; Kennedy, B. J., Synchrotron X-ray diffraction study of the $Ba_{1-x}SrSnO_3$ solid solution. *Journal of Solid State Chemistry* **2013,** *200*, 241-245.
13. Kennedy, B. J.; Qasim, I.; Knight, K. S., Low temperature structural studies of $SrSnO_3$. *Journal of Physics: Condensed Matter* **2015,** *27*, 365401.
14. Monkhorst, H. J.; Pack, J. D., Special points for Brillouin-zone integrations. *Physical Review B* **1976,** *13* (12), 5188-5192.
15. Albuquerque, A. R.; Bruix, A.; dos Santos, I. M. G.; Sambrano, J. R.; Illas, F., DFT Study on Ce-Doped Anatase TiO2: Nature of Ce^{3+} and Ti^{3+} Centers Triggered by Oxygen Vacancy Formation. *The Journal of Physical Chemistry C* **2014,** *118* (18), 9677-9689.
16. Lucena, G. L.; Lima, L. C. d.; Honório, L. M. C.; Oliveira, A. L. M. d.; Tranquilim, R. L.; Longo, E.; Souza, A. G. d.; Maia, A. d. S.; Santos, I. M. G. d., $CaSnO_3$ obtained by modified Pechini method applied in the photocatalytic degradation of an azo dye. *Cerâmica* **2017,** *63*, 536-541.
17. Sales, H. B.; Bouquet, V.; Députier, S.; Ollivier, S.; Gouttefangeas, F.; Guilloux-Viry, M.; Dorcet, V.; Weber, I. T.; de Souza, A. G.; dos Santos, I. M. G., $Sr_{1-x}Ba_xSnO_3$ system applied in the photocatalytic discoloration of an azo-dye. *Solid State Sciences* **2014,** *28* (Supplement C), 67-73.

18. de Andrade, F. V.; de Lima, G. M.; Augusti, R.; da Silva, J. C. C.; Coelho, M. G.; Paniago, R.; Machado, I. R., A novel TiO_2/autoclaved cellular concrete composite: From a precast building material to a new floating photocatalyst for degradation of organic water contaminants. *Journal of Water Process Engineering* **2015,** *7*, 27-35.
19. Moreira, E.; Henriques, J. M.; Azevedo, D. L.; Caetano, E. W. S.; Freire, V. N.; Albuquerque, E. L., Structural, optoelectronic, infrared and Raman spectra of orthorhombic $SrSnO_3$ from DFT calculations. *Journal of Solid State Chemistry* **2011,** *184* (4), 921-928.
20. Lee, C. W.; Kim, D. W.; Cho, I. S.; Park, S.; Shin, S. S.; Seo, S. W.; Hong, K. S., Simple synthesis and characterization of $SrSnO_3$ nanoparticles with enhanced photocatalytic activity. *International Journal of Hydrogen Energy* **2012,** *37* (14), 10557-10563.
21. Libralato, G.; Prato, E.; Migliore, L.; Cicero, A. M.; Manfra, L., A review of toxicity testing protocols and endpoints with Artemia spp. *Ecological Indicators* **2016,** *69*, 35-49.